Chapter 10
Physical Virology with Atomic Force and Fluorescence Microscopies: Stability, Disassembly and Genome Release

María Jesús Rodríguez-Espinosa, Miguel Cantero, Klara Strobl, Pablo Ibáñez, Alejandro Díez-Martínez, Natalia Martín-González, Manuel Jiménez-Zaragoza, Alvaro Ortega-Esteban, and Pedro José de Pablo

Abstract The core of Atomic Force Microscopy (AFM) is a nanometric tip mounted at the extreme of a microcantilever that scans the surface where the virus particles are adsorbed. Beyond obtaining nanometric resolution of individual viruses in liquid environment, AFM allows the manipulation of single particles, the exploration of virus biomechanics and to monitor assembly/disassembly processes, including genome release in real time. This chapter starts providing some inputs about virus adsorption on surfaces and imaging, including an example of tip dilation artifacts. Later, we exemplify how to monitor the effects of changing the chemical environment of the liquid cell on TGEV coronavirus particles. We go on by describing approaches to study genome release, aging, and multilayered viruses with single indentation and mechanical fatigue assays. The chapter ends explaining an AFM/fluorescence combination to study the influence of crowding on GFP within P22 bacteriophage capsids.

M. J. Rodríguez-Espinosa · M. Cantero · K. Strobl · A. Díez-Martínez · M. Jiménez-Zaragoza · A. Ortega-Esteban · P. J. de Pablo (✉)
Departamento de Física de La Materia Condensada, Universidad Autónoma de Madrid, 28044 Madrid, Spain
e-mail: p.j.depablo@uam.es

M. J. Rodríguez-Espinosa
Department of Structure of Macromolecules, Centro Nacional de Biotecnología, (CNB–CSIC), Darwin 3, 28049 Madrid, Spain

P. Ibáñez
Department of Theoretical Physics of Condensed Matter, Universidad Autónoma de Madrid, Cantoblanco Campus, 28049 Madrid, Spain

N. Martín-González
AFMB UMR 7257, Aix Marseille Université, CNRS, Marseille, France

P. J. de Pablo
Solid Condensed Matter Institute IFIMAC, Universidad Autónoma de Madrid, 28049 Madrid, Spain

M. Comas-Garcia and S. Rosales-Mendoza (eds.), *Physical Virology*, Springer Series in Biophysics 24, https://doi.org/10.1007/978-3-031-36815-8_10

Keywords Atomic force microscopy · Force curve · Nanoindentation · Beam deflection · Tip · Cantilever · Stylus · Topography · Aqueous solution · Mechanical fatigue · DNA condensation · Assembly · Disassembly

Introduction

Viruses are outstanding examples of how the Nature evolution can achieve sophisticated systems designed to last with minimalistic resources [1]. They can be considered as nanomachines whose function and properties are not only interesting for understanding their biology, but also for applications in material science [2]. In this vein, the mechanical properties of biomolecular complexes are essential for their function, and viruses are not an exception [3]. Virus structures exhibit certain meta-stability whose modulation permits fulfilling each task of the viral cycle on time thanks to their physicochemical properties. The basic construction of non-enveloped viruses consists of the capsid, a shell made up of repeating protein subunits (capsomers) or lipids, packing within the viral genome [1]. Far from being static structures, both enveloped and non-enveloped viruses are highly dynamic complexes that shuttle and deliver their genome from host to host in a fully automatic process. These natural designed capabilities have impelled using viral capsids as protein containers of artificial cargoes (drugs, polymers, enzymes, minerals) [2] with applications in biomedical and materials sciences. Both natural and artificial protein cages have to protect their cargo against a variety of physicochemical aggressive environments, including molecular impacts in highly crowded media [4], thermal and chemical stresses [5], and osmotic shocks [6]. Thus, it is important to use methodologies that supply information about protein cages stability not only under different environments, but also its evolution upon structural changes. Structural biology techniques such as electron microscopy (EM) and X-ray are used to unveil the structure–function interplay, revealing high resolution structures of protein cages [7]. However, these methodologies require a heavy average of millions of particles present in the crystal (X-ray) or thousands of structures for the model reconstruction (cryo-EM). Thus, they provide limited information on possible structural differences between individual particles that differs from the average structure. In addition, these approaches require conditions (i.e., vacuum) far away of those where protein shells are functional (liquid), precluding the characterization of protein shells dynamics and properties in real time. Indeed, the advent of single molecule technologies has demonstrated that mechanical properties of biological molecular aggregates are essential to their function [8]. The exploration of these properties would complement the structural biology methodologies (EM and X-ray) to find the structure–function-property interplay of virus structures. Atomic Force Microscopy (AFM) may not only characterize the structure of individual protein-made particles in liquid milieu, but also to obtain physicochemical properties of each one [9]. In addition, the nano-dissection abilities of AFM allows the local manipulation of protein shells to learn about their assembly/disassembly [10]. In this chapter, we give a general overview of how to

apply AFM methods to protein shells. Our tour starts with a basic review of the recipes for attaching protein cages to solid surfaces. Afterwards we describe some modes for imaging protein shells with AFM and comment on inherent artifacts, such as geometrical dilation. We describe the ability of AFM to explore virions under changing environments in the liquid cell. Subsequently we describe the nanoindentation methodology, which probes the stiffness, breaking force, brittleness, and cargo unpacking of individual protein shells. Afterwards we focus on the effects of cyclic loading on individual particles (disassembly), and the AFM/fluorescence combination for exploring protein cages packing GFP.

Insights on AFM Methodology

Cantilevers. In AFM a microcantilever with a nanometric tip located at the very extreme actuates as a force transducer which palpates the viruses adsorbed on a solid surface. Cantilevers with different spring constants are mounted on a chip. For example Olympus OMCL-RC include a variety of four spring constants: 0.39, 0.76, 0.05 and 0.10 N/m that can be used with different viruses, depending on their stability and the adsorption strength to the surface. Figure 10.1a shows and optical microscopy image of the 0.05 N/m cantilever where the pyramid tip is encircled. Olympus stopped the production of OMCL-RC cantilevers. PNP-DB and QP-BioAC tips (Nanoandmore™) with similar properties can be used. The chip holding the cantilever is attached to the quartz window of the liquid cell which is created between the surface and the cantilever holder (Fig. 10.1b). For the shake of comparison with viruses, Tetraspeck™ (Thermofisher) plastic spheres of 100 nm in diameter are spread on a glass surface that are seen as white blobs with a size of ~250 nm because of the diffraction limit.

Immobilization of virus particles on surfaces. Virus particles are adsorbed to the surface by using physical forces (physisorption) with the substrate, including polar, non-polar, an van der Waals interactions [11]. Physisorption traps virus particles without inducing chemical bonds that might alter their structure [12]. Each virus species has individualized features such as local charge densities or hydrophobic patches [13] that can be used for anchoring the particles, via hydrophobic and/or electrostatic interactions, on different materials, such as glass, mica and HOPG (Highly Oriented Pyrolytic Graphite). Mica and HOPG surfaces are layered materials whose preparation consist of removing the last layer with adhesive tape, exposing a fresh surface ready for experiments. Care should be taken on leaving a flat surface by avoiding dangling whiskers on the area of the meniscus because they might crash with the cantilever. HOPG presents a non-polar surface and protein cages adsorb via hydrophobic interactions [14]. In the case of human adenovirus (HAdv) virus particles can be adsorbed on HOPG, silanized glass and mica with different results. HOPG collapses most of HAdv particles, indicating a strong non-polar (hydrophobic) interaction. However, silanized glass [9] reduces the attachment interaction and

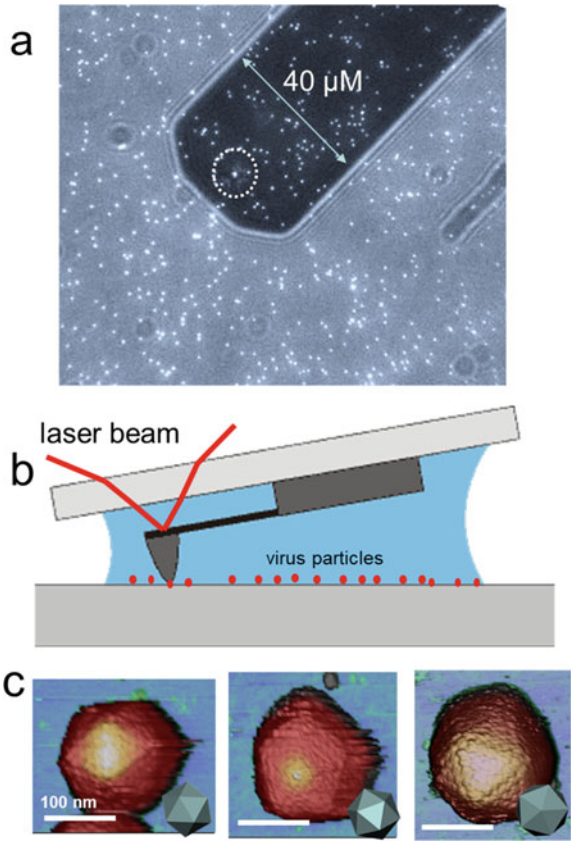

Fig. 10.1 Attaching protein shells on surfaces. **a** Optical microscopy image of an 0.05 N/m OMRC cantilever, with the encircled tip. Plastic bead of 100 nm in diameter are adsorbed on the surface for the sake of comparison. **b** Cartoon of the liquid cell. Protein cages and cantilever are not in scale. **c** HOPG, glass and mica bare substrates before attaching the viruses. **d** hAdV particles on HOPG, glass and mica. **e** Individual hAdV particles showing twofold, threefold and fivefold symmetry orientations

allows imaging intact icosahedral particles exhibiting fivefold, twofold and threefold symmetry orientations on the surface (Fig. 10.1c). Interestingly, using $NiCl_2$ 150 mM on mica [11] induce the adsorption of HAdv particles only at the threefold symmetry orientation, thus protein particles exhibit a triangular facet (Fig. 10.1c, right). Adsorption of virus particles on surfaces also may induce a reduction of the particle height [15, 16]. From a practical point of view predictions on proteins shells adsorption are difficult to make, and one uses the try-and-error methodology to find the best conditions.

Imaging. In AFM the tip scans the sample in x, y and z directions by using piezo actuators. While x and y scanners move in a pre-established way over a square region, the cantilever bends following the surface topography. Either the cantilever deflects

perpendicularly to the surface applying a normal force (F_n) (Fig. 10.2a), or it bends laterally by torsion exerting a dragging force parallel to the surface (F_l) (Fig. 10.2b). Both F_n and F_l are monitored by focusing a laser beam at the end of the cantilever, whose reflection is registered in a four-quadrant photodiode. Thus, each pixel of the image located at a particular position of the planar coordinates (x, y), will be associated with certain bending values of the cantilever F_n and F_l. If the particle is not strongly enough attached or if it is too soft, it can be swept or modified under large bending forces. To avoid this effect as much as possible, a feedback loop is engaged to F_n to move the z piezo position in such way that F_n is kept constant. In this operational approach (contact mode, Fig. 10.2c), the AFM topography map will have x, y and z coordinates. The torsion F_l of the cantilever exerts about 40 times the perpendicular bending force F_n [17]. Individual virus particles are thus susceptible to undesired modifications by lateral forces. Their size of tens of nanometers offers a large topographical aspect ratio that is difficult to track by the feedback loop. A typical approach for surpassing this limitation is using fixation agents, such as glutaraldehyde. In such conditions AFM provide images whose resolution is comparable to that of some EM images [18]. Nevertheless, since glutaraldehyde structurally reinforces the specimens [19, 20], it precludes any characterization of dynamics or properties of intact native viruses, such as assembly/disassembly or physical properties [21]. Other approaches include developing imaging modes that avoid dragging forces as much as possible. In jumping mode (JM) [22], the lateral tip displacement occurs when the tip and sample are not in mechanical contact, thereby avoiding shear forces to a large extent (Fig. 10.2d). JM performs consecutive approach-release cycles at every pixel of the sample. In each cycle, known as force vs. distance z curve (FZ, Fig. 10.2e), the z-piezo approaches tip and sample from non-contact (label 1 at Fig. 10.2e) until establishing mechanical contact (label 2 at Fig. 10.2e) and reaching a certain feedback force (label 3 at Fig. 10.2e). After a few milliseconds, the z-piezo retracts about 100 nm until releasing the tip from the surface (label 1 at Fig. 10.2e). Subsequently the scanner moves laterally to the next pixel, and the process starts again. An AFM cantilever experiences a viscous drag while moving up and down in liquid, giving rise to a hysteresis loop (Fig. 10.2e) because forward and back curves do not coincide. Although AFM dynamic modes have also able of imaging protein shells in liquid conditions, it is difficult to control the applied force [23].

Tip dilation. The typical radius of the tip apex for usual cantilevers (OMCL-RC800PSA) is ~20 nm, and it is comparable to the curvature of the virus particles diameter. In this case, tip size plays an important role on the image resolution by inducing a lateral expansion, namely dilation, of the specimen [24]. Since dilation very often impairs high resolution in proteins, it is convenient to estimate how the tip-size is going to affect to AFM images. WSxM software [25] implements a geometrical dilation algorithm that allows simulating the dilation of protein shell's structure. By using Chimera software [26] it is possible to access to a particular protein shell structure, such as the electron microscopy model. The "Surface Color By Height" option generates a gray-scale image that captures the topography variation in a given orientation. The TIFF format of this image can be imported by WSxM software and calibrated (www.wsxm.eu). The dilation algorithm input is the tip radius, and the

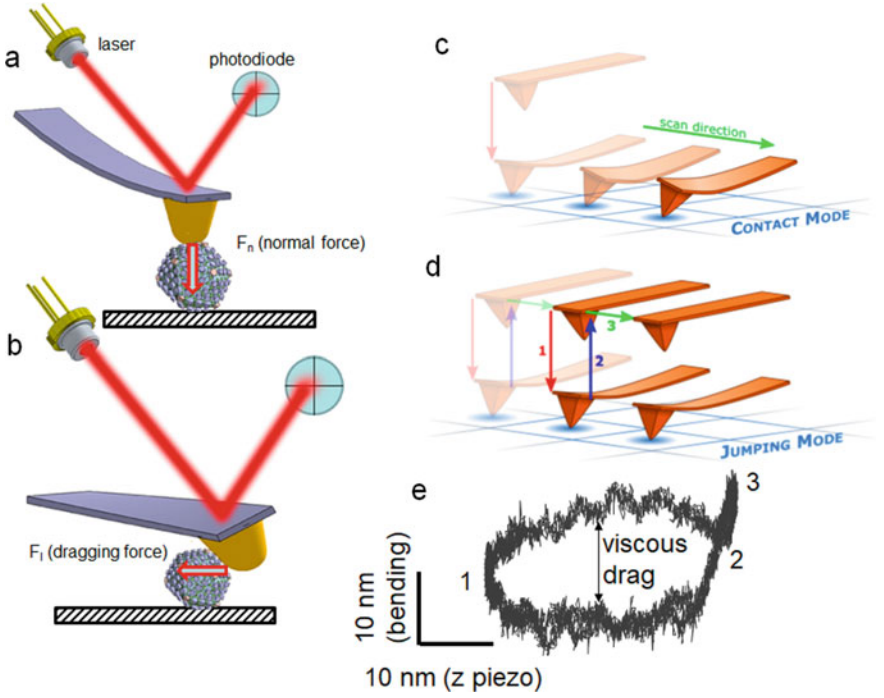

Fig. 10.2 AFM working modes. **a** and **b** show the normal (F_n) and lateral forces concepts, respectively. **c** and **d** indicate contact and jumping modes, respectively. **e** Force curve of jumping mode in liquids, indicating the viscous drag and the important stages (see text)

dilated structure is calculated. Figure 10.3 exemplifies the dilation of phi29 bacteriophage EM structure [27]. Figure 10.3a shows the 3D rendered topography data of a bacteriophage phi29 on HOPG. By using the dilation algorithm with a 10 nm in diameter tip on the PDB model of phi29 phage [27] it is possible to obtain the dilated topography (Fig. 10.3b). Dilation strongly depends on the tip size, as shown in Fig. 10.3c. The darker area of Fig. 10.3b represents the extra dilated geometry of phi29 around the electron microscopy model (light colored).

Applications

Imaging at different environment conditions. The conditions of the liquid environment in the liquid cell can be gradually changed for monitoring the stability of virus capsids over time. One pump connected to the inlet of the chamber inserts the buffer at the desired final concentration, and another pump connected to the outlet withdraws liquid at the same velocity of the inlet. In this particular case (Fig. 10.4) we observe the effect of a non-ionic detergent (IGEPAL® CA-630 (Sigma-Aldrich,

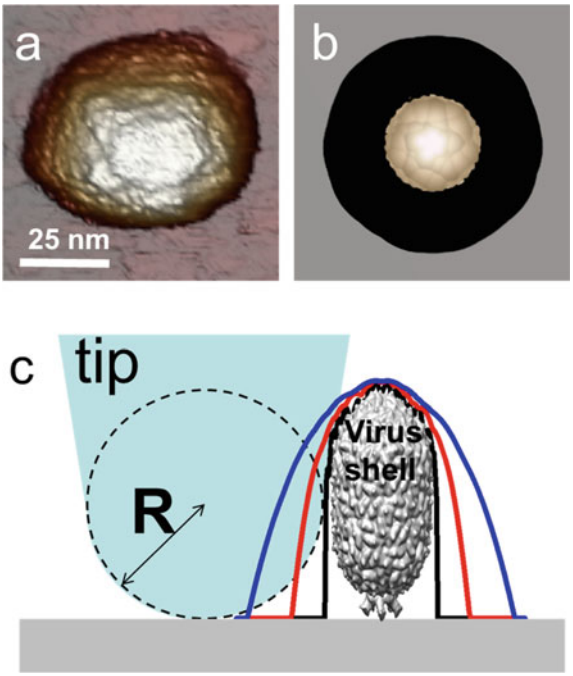

Fig. 10.3 Dilation effects in the phi29 bacteriophage shell. **a** represents the AFM image of a prohead. In **b** the bright color illustrates a EM structural model of phi29, and the dark area indicates the dilation corresponding to a tip of 10 nm in diameter. The cartoon of **c** indicates the dilation as a function of the tip size: dark, red and blue curves are the topographical profiles obtained with tips of 0.5 nm, 5 and 10 radius in diameter, respectively

Saint Louis, MI, USA, CAS: 9002-93-1)) on the structure of the coronavirus *transmissible gastroenteritis virus* (TGEV) [28], whose structure [29] and mechanical properties [30] are identical to SARS-CoV-2. Consecutive images of the same TGEV virus particle while increasing IGEPAL concentration in the liquid cell were taken (Fig. 10.4a). This virus was continuously imaged more than 40 times while IGEPAL was increased up to ~0.06% for 80 min. The virus particle remained stable at 0.020% IGEPAL, although at 0.023% some deterioration could be recognized. In frame #26, some material was ejected from the virus and a circular crack at the top appears. This damaged structure seems stable until frame #40. For statistical analysis, the height data evolution of eight particles subjected to similar process are plotted their individual (Fig. 10.4b, thin grey) and their average (Fig. 10.4b, thick dark) height variation over time. Consecutive images of virions in buffer without detergent were taken as control (Fig. 10.4b, blue), showing that their heights were not affected by AFM scanning. Figure 10.4c shows the effect of the pH variation on the stiffness of human adenovirus particles [31].

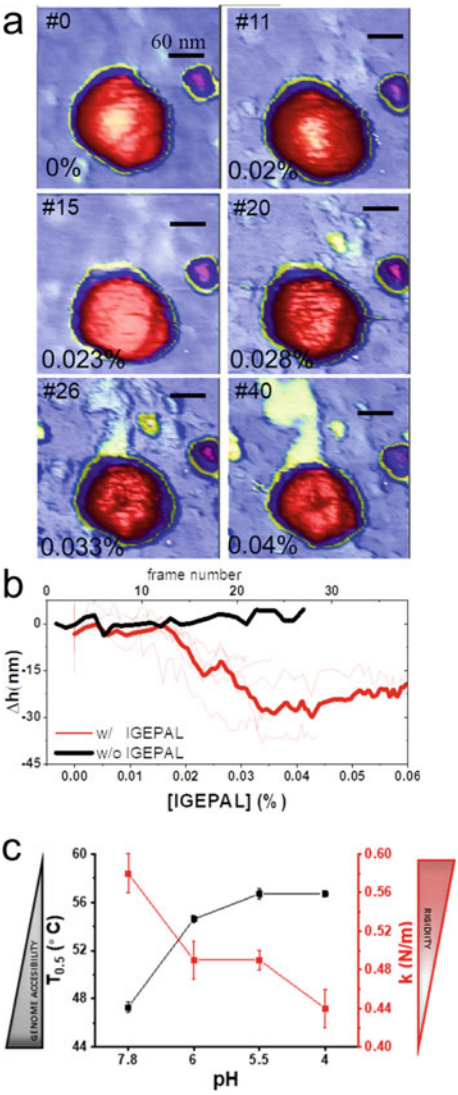

Fig. 10.4 Imaging while changing the environment in the liquid cell: effect of IGEPAL concentration on TGEV virions. **a** Topographical images were taken while the concentration of IGEPAL was increased over time. The frame number is shown in the upper left corner and the concentration of IGEPAL in the bottom-right. **b** Height loss during the time course assay. Experimental curves are shown in light red and the average curve of 8 observations is shown in red. As a control, the height of 1 virus particle without detergent is shown (black). Adapted from [32]. **c** Evolution of the spring constant with pH in human adenovirus. Adapted from [31]

Mechanical properties of viruses: nanoindentation. Single force curve (FZ) experiments consist on pushing on the top of a selected protein shell (Fig. 10.5a). The FZ is executed on the particle at a typical speed of 50 nm/s to allow the water leaving the virus when it is squeezed [33]. After the contact between tip and particle is stablished, FZ typically shows an approximate linear behavior, which corresponds to the elastic regime of the shell and ascribes to the mixed bending of the cantilever and sample deformation (Fig. 10.5a, b, label 2). When the z-piezo elongation surpasses the critical indentation, particle breaks (Fig. 10.5, 1.1 nN) inducing a drastic decrease of the force, that resemble the penetration of the tip apex trough the virus (Fig. 10.5a, b, label 3). Afterwards the FZ is linear again and represents the cantilever bending on the solid substrate. By performing a FZ on the substrate (Fig. 10.5b, dotted line) and assuming that it is much more rigid that the cantilever, we can obtain the cantilever deformation. In this case, the human picobirnavirus particle [34] yields and breaks after the nanoindentation experiment (Fig. 10.5c). The subtraction of sample from substrate curves allows isolating the deformation of the virus cage (Fig. 10.5d). From these data we can obtain a few mechanical parameters: Fitting of the elastic part from 0 to 5 nm results in the stiffness or spring constant of virus shell (k = 0.25 N/m). The breaking or yield force is the force value when the elastic regime finish at 5 nm of indentation (F_b = 1.1 nN). The critical indentation δ_c, is the deformation of the virus when it breaks (5 nm). Thin shell theory relates the protein shell stiffness with the Young's modulus as $k \approx E\frac{h^2}{R}$, where h is the thickness of the shell and R its radius [35]. The area enclosed between forward and backward curves from indentation 0 up to 5 nm is the energy used to break the cage. In this case, it is about 8.8 nm × nN, i. e. 8.8 × 10^{-18} J or 2140 k_BT, which approaches the order of magnitude of the total energy used for assembling the virus [36]. In addition, the critical strain $\varepsilon_c = \delta_c/h$, where h is the initial height of the protein cage as measured with AFM, informs about the brittleness or the mechanical stability of protein cages [15]. In this case, ε_c = 5/36 = 0.14, saying that the particle breaks when it is deformed 14%.

Genome externalization and mechanical properties of cargo. Nanoindentations at low force can induce cracks, allowing the access to the inner cargo of viruses. For instance, the consecutive application of nanoindentation cycles in HAdv cracks-open the shell in a controlled fashion to probe the mechanical properties of the core [37, 38]. These mechanical properties relate with the condensation state of dsDNA. In particular, the HAdv core is formed by 35 kbp dsDNA molecule bound to positively charged viral proteins that constitute ∼50% of the core molecular weight. Approximately about 500–800 copies of protein VII (pVII) contributes with 22 kDa to the core, becoming the majority protein. Consecutive nanoindentation experiments (Fig. 10.6) performed on wild type (HAdv-wt) and mutant lacking pVII (HAdv-PVII-) human adenovirus particles provide information on the pVII function. Figure 10.6a presents the typical evolution of HAdv-wt and HAdv-VII– particles in a multiple indentation experiment. The first indentation (FIC#0) on the intact shell (Fig. 10.6a, #0) opens a crack at the icosahedral facet with a similar size to the apex of the AFM tip (∼20 nm) (Fig. 10.6a, #1), allowing a direct access of the tip to the

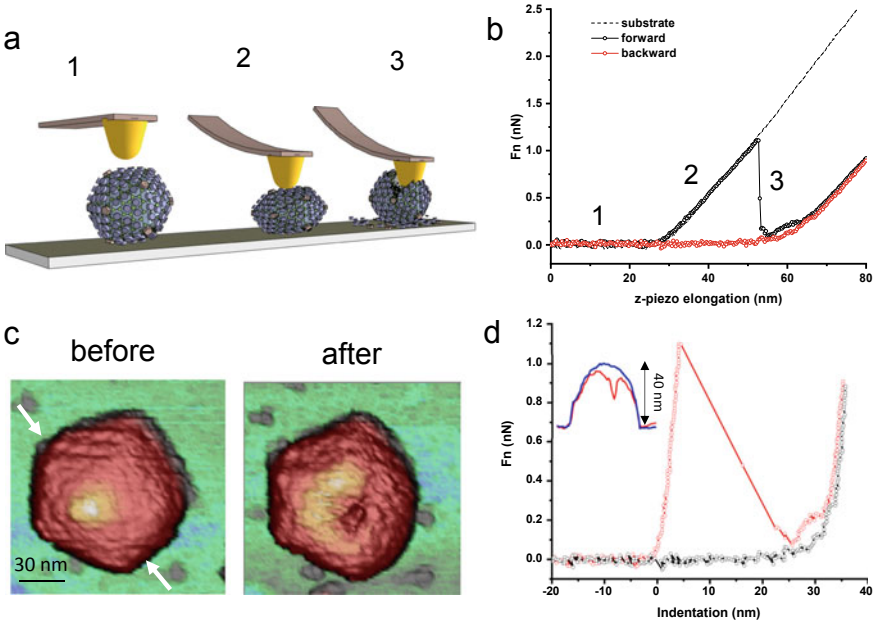

Fig. 10.5 Single indentation assay. **a** Cartoon showing the three main stages during nanoindentation experiment on a protein cage: before contact (1), during deformation (2) and after breaking (3). **b** Evolution of F_n along the z-piezo elongation. Forward curve exhibits the three stages commented in **a**. **c** AFM topographies before and after nanoindentation showing a crack. **d** Nanoindentation data extracted from **b**, showing the shell deformation. Inset compares topographical profiles before (blue) and after (red) de experiment obtained at the line marked by the arrows in **c**. Inset shows the profile of the particle

core. Subsequent indentations present a non-linear Hertzian behavior in contrast with the linear deformation found in intact particles (Fig. 10.5). During the first indentation after capsid cracking (Fig. 10.6a, #1), HAdv-wt cores are not deformed beyond 40 nm at 3 nN, while HAdv-VII– cores undergo larger indentations, up to ~60 nm, at forces as low as 2 nN (Fig. 10.6b). This difference indicates that it is easier for the AFM tip to penetrate/deform HAdv-VII– than HAdv-wt cores. That is, in the absence of protein VII the HAdv core is softer and less condensed. Elongated structures with a height compatible with dsDNA strands (Fig. 10.6a, yellow) appeared on the substrate surrounding HAdv-VII– particles after the first fracture of the shell (Fig. 10.6a, #1, top), but not in HAdv-wt (Fig. 10.6a, #1, bottom). Material consistent with unpacked DNA seemed to be more abundant in HAdv-VII– particles that in HAdv-wt for the equivalent indentation number (Fig. 10.6a). This qualitative observation suggests that it is easier to exit the disrupted shell for the VII-free genome than for the VII-bound one. An alternative possibility would be that the VII-free genome has a larger tendency to adsorb to the mica substrate than the VII-bound DNA. Measurements of the topographical profile across the crater produced by the successive indentations (Fig. 10.6c) support the first possibility. Because

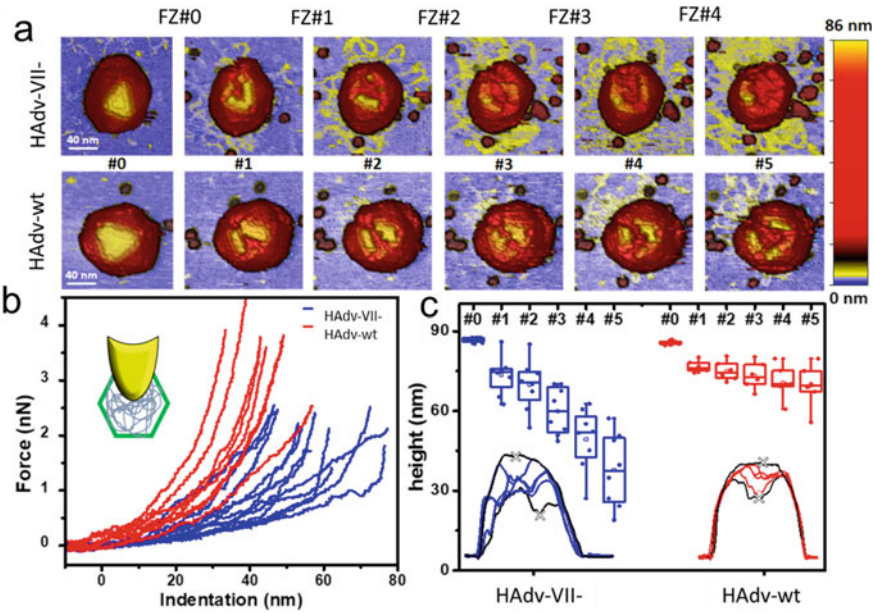

Fig. 10.6 Mechanical properties of human adenovirus core: the role of protein VII. **a** Images showing the evolution HAdv-wt and HAdv-VII– particles during multiple indentation assays. Images are colored by height, as indicated by the color bar at the right hand side. **b** FZ curves corresponding to the first indentation performed on the core of 8 HAdv-wt (red) and 12 HAdv-VII– (blue) particles. **c** Evolution of the core height (as indicated by the minimum height in the crater, grey crosses) for eight HAdv-VII– and six HAdv-wt particles. Insets: Examples of topographical profiles obtained through the crater opened by the indentation Adapted from [38]

topographical profiles include both the crater and rims, we used the lowest height inside the crack as an indicator of the remaining core contents (Fig. 10.6c, insets). Plotting the evolution of this parameter along six consecutive indentations for eight HAdv-VII– and six HAdv-wt particles (Fig. 10.6c) showed that, indeed, the core components are leaving faster the HAdv-VII– than the HAdv-wt cracked particles [38]. The application of consecutive indentations to coronavirus structures (TGEV), also inform about stability and genome release [32]. These experiments unveiled two different behaviors of TGEV particles: In the first case (Fig. 10.7a), a virus particle was probed seven times with maximum forces ranging from 0.6 to 3 nN, remaining unaltered through the alternating AFM images. In fact, ~65% of the explored virus particles (N = 69) kept their height constant (Fig. 10.7c, black), indicating that their structure was elastic and not affected by the nanoindentations. However, in the second case (Fig. 10.7b) and using the same FZ number and parameters, the TGEV particle showed evident structural changes consisting of appearing a circular crater after the first FZ that enlarged after consecutive deformations until the virus appears to have been ripped open, releasing its content (Fig. 10.7, #7). This behavior was observed in ~35% of the explored particles and was accompanied by a gradual decrease in height

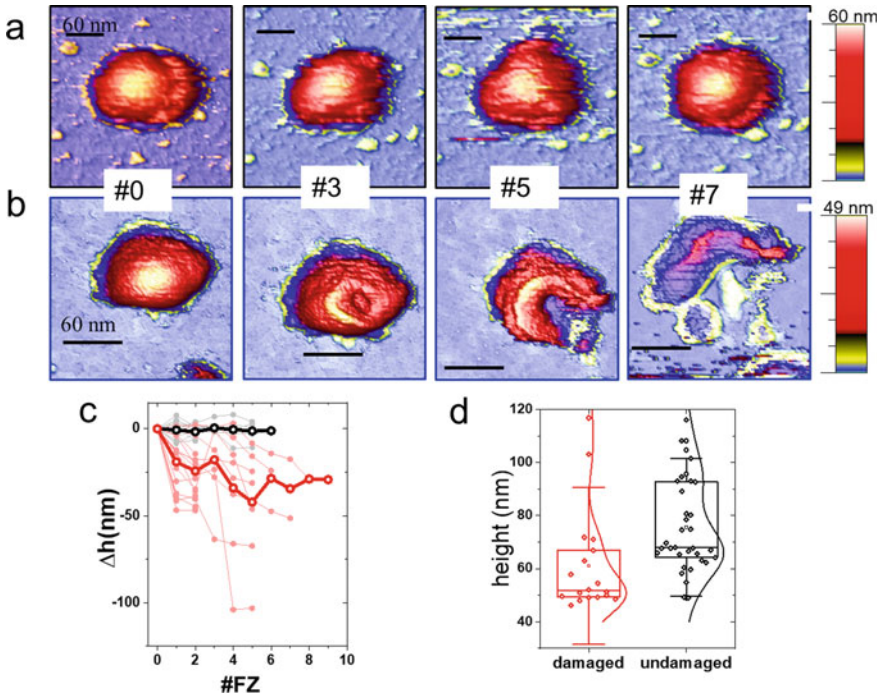

Fig. 10.7 Mechanical properties of TGEV coronavirus: the role of packing fraction. **a** and **b** present topographical images of TGEV virions after consecutive indentations. Particles can be classified in two groups: indentation resistive (**a**) and indentation sensitive (**b**) as shown in the topo images. Frame number indicates how many indentations were performed. **c** Chart evolution of virus height as a function of the indentation number (FZ#). The values of height are taken from the indented region. Black and red charts represent indentation resistive an indentation sensitive, respectively. **d** Height box-plot distribution of intact virus particles. Adapted from [32]

after each indentation (Fig. 10.7c, red). It is important to remark that the initial height of the particles that remained undamaged (indentation resistive) was larger than the damaged ones (indentation sensitive) (Fig. 10.7d), a difference that was significantly different at a 95% level of confidence. By assuming that all viruses package the same amount of genome, it is likely that everyone contains a similar number of RNPs, no matter their size. Therefore, the larger height of these particles (Fig. 10.7d) suggests a loosened core state represented by the 'eggs-in-a-nest' assembly [39]. In this case, when the tip retracts, RNPs recover their original positions and the flexible membrane returns to its previous height. In contrast, indentation-sensitive particles (Fig. 10.7b) exhibited lower heights than the resistive ones (Fig. 10.7d). The particle crack-opened with a permanent fracture (Fig. 10.7b) of ~25 nm in depth (Fig. 10.7c, blue). The lower height indicates a higher packing fraction ('pyramid' packing) [39] without internal free room, preventing the RNPs from rearranging under the mechanical stress induced by the tip. In fact, structural data of SARS-CoV-2 indicate this 'pyramid' packing occupies ~36% of the cavity, very close to viruses

with high packing fraction values, such as lambda and phi29 bacteriophages [40]. Together with the AFM tip, solidly packed RNPs act as a "hammer and anvil" on the membrane, concentrating the mechanical stress on the virus envelope and causing permanent fractures (Fig. 10.7b). Consecutive imaging of the virus particles after each nanoindentation (Fig. 10.7b) reported increasing damage, with virus height loss from 25 to 100 nm (average decrease ~40 nm; Fig. 10.7c, red).

Mechanical fatigue, disassembly and aging. The breaking force describes the largest force that the virus can survive. Single indentation experiments collapse the particle by inducing large and uncontrollable changes in its structure. It is thus difficult to derive consequences about disassembly, since in the cycle of many virus shells, for instance, disassembly takes place by losing individual capsomers in an gradual way [41]. A protein cage must also resist a constant barrage of sub-lethal collisions in crowded environments [42]. Equipartition theorem provides an estimation of the energy transferred in a molecular collision to be $\sim\frac{3}{2}k_BT$, which is far below that the energy supplied by single indentation assay experiments. Imaging of individual protein shells with AFM in jumping mode requires thousands of load cycles (FZs) at low force (~100 pN per pixel, Fig. 10.2c) [22]. A rough estimation indicates that ~10 k_BT is transferred to the particle at every cycle [43], very close to the molecular collisions value. The continuous imaging of a particle enables the evaluation of any structural alteration while subjected to cycle load at low forces. Mechanical fatigue experiments have demonstrated to be a disassembly agent able of recapitulating the natural pathway of adenovirus uncoating [22]. Therefore fatigue provides additional information by providing information on shell stability under multiple deformation cycles at low force (~100 pN) [44], well below the breaking force (Fig. 10.5d). Let us exemplify the mechanical fatigue methodology in the case study of HAdv [45]. This virus travels to the cytoplasm until the nuclear pore to deliver its genome. Inside the host cell, the virus finely tunes the sequential loss of pentons (proteins located at the icosahedron corners) to render a semi disrupted capsid at the nuclear pore. Viruses with too many pentons would not be able to release their DNA through the cell's nuclear pore, whereas those with too few pentons would liberate their genome before reaching the nucleus. Mechanical fatigue induces penton failure [44] (Fig. 10.8a), which mimics the stresses the virus sustains during its journey to the nucleus. This approach allows to study the transition kinetics of penton release as a two-state process, from where it is possible derive the spontaneous escape rate and the free energy barrier of a penton [45]. Moreover, fitting the survival probability P of penton N (Fig. 10.8b) under different fatigue forces to Weibull analysis: $P(N) = 1 - \exp\left[-\left(\frac{N+1}{\lambda}\right)^{\beta}\right]$, where λ is the half-life and β determines the nature of the penton's dynamics release. In particular, $\beta < 1$ would imply that failure rate decreases over time (*Lindy effect*). This effect can be found in ancient monuments, since the older something is, the more likely it will survive. The case of $\beta = 1$ would imply a Poisson process with a constant probability of penton failure over time. However, $\beta > 1$ (Fig. 10.8b) involves the phenomenon termed in materials science as *aging*, which means that the failure rate increases over time. This indicates that the probability for the virus of losing a penton increases if other

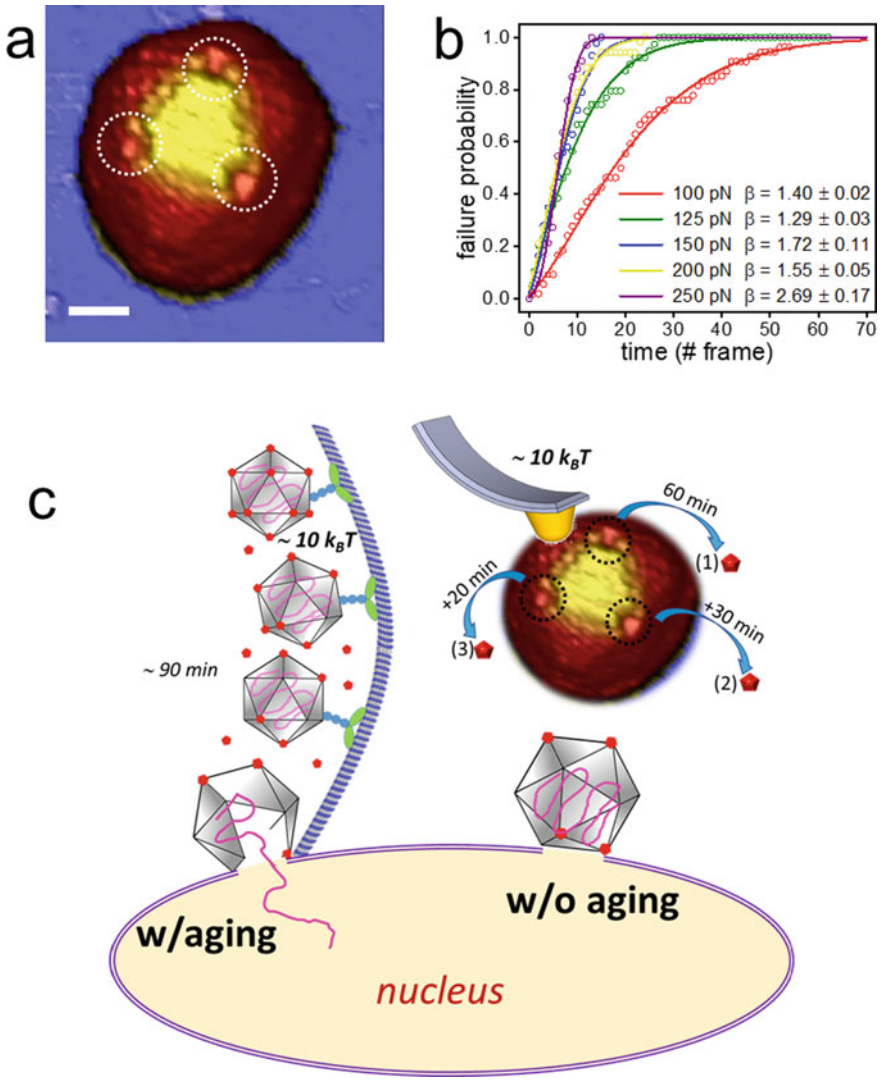

Fig. 10.8 Mechanical fatigue and aging of human adenovirus. **a** AFM of a HAdv particle showing three vacancies of pentons on the triangular facet (encircled). **b** Failure probability of pentons overt time for different forces. Inset show the fitting parameters of Weibull statistics. **c** Diagram showing the biological implications of aging on the virus infectivity (see text). Adapted from [45]

penton has been lost before. This aging process ($\beta > 1$) accelerates the overall penton escape rate by about 50% (Fig. 10.8c) with respect to a sequence of independent escape events ($\beta = 1$). Specifically, while the first penton resists about 60 min, the second and third would last 30 and 20 min more, respectively (Fig. 10.8c). In this way, *aging* guarantees to have the virus particle just disrupted enough to release the

genome trough the nuclear pore. Without aging, virus particle would be still quite complete and the genome could not escape (Fig. 10.8c), with negative consequences for infection.

Layer-by-layer disassembly of a multilayered virus with mechanical fatigue. Several viruses wrap their genome in several layers of protective casing, resulting in an onion-like structure. For example, the rotavirus (RV), that can induce severe diarrhea in young children, have three layers built of different proteins with various functionalities. Rotavirus subparticles may exist with only one or two of these coats, which allows to study each layer in detail [46]. Mechanical fatigue allows to explore the strength and binding of each layer (Fig. 10.9a). The RV infectious particle is a 100 nm non-enveloped triple-layered particle (TLP) composed of three concentric protein shells enclosing the dsRNA genome and the viral RNA polymerase and capping enzyme. The inner layer surrounds the eleven dsRNA genomic segments associated with the RNA-dependent RNA-polymerase VP1 (125 kDa) and the RNA-capping enzyme VP3 (88 kDa) at the pentameric positions. This thin single-layered particle (SLP), an intermediate structure that is involved in the packing and replication of the viral genome, is surrounded by a thick layer formed by 260 VP6 pear-shaped trimers (45 kDa) in the double-layered particle (DLP). This particle, which does not disassemble during the infection, constitutes the transcriptional machinery that initiates the core steps of the viral replication cycle once delivered in the host cell cytoplasm. Cyclic imaging of the TLP (Fig. 10.9b, left) at forces between 100 to 200 pN per pixel shows that, while the VP4 spikes are removed from the particle surface in a few frames (Fig. 10.9b, middle), the VP7 layer remains mostly intact (Fig. 10.9b, right) during 80 frames (light red in Fig. 10.9f). These results illustrate that the spikes are easily removed by the AFM tip and are not strongly anchored. However, the VP7 layer displays a strong resistance against fatigue. A strong binding energy between capsomers would not only result in a high resistance of individual proteins against fatigue, but also will contribute to a high breaking force when all capsomers are probed in a single indentation assay experiment [46]. The current model proposes a calcium concentration drop in endosomal compartments during RV entry as the factor that triggers VP7 disassembly and membrane penetration. In fact, calcium depletion by chelating agents (as EDTA) is used to uncoat TLP to DLP by inducing VP7 trimer dissociation. To explore the structural consequences of this process in real time, fatigue assays are carried out on TLP while EDTA simultaneously flowed in the AFM liquid chamber, to induce the gradual depletion of Ca ions of the particles (Fig. 10.9c). In these conditions, fatigue induces the neat VP7 detachment from the VP6 subjacent layer (indicated by a circle in Fig. 10.9c, #19) even before the spikes are removed. Indeed, the evolution of the topographic profiles (dark red in Fig. 10.9f) show abrupt downwards steps very close to the VP7 thickness (red arrow of Fig. 10.9f) indicating that TLP particle loses VP7 completely while keeping VP6. These results not only suggest that Ca ions mediate the interaction between VP7 and VP6 layers, but also that the absence of ions weakens the interaction between VP7 subunits. If fatigue continues, VP6 subunits are neatly removed from VP2 layer (circle in Fig. 10.9c, #29). Therefore, VP6 layer appears forming a weak shell whose interaction with the beneath VP2 layer is not very strong, since it peels off rapidly to reveal the SLP. Similar results are found on DLP. Again, fatigue induced a clean VP6 disassembly

after less than 10 frames (circle in Fig. 10.9d, #8). In this case the evolution of the topographic profiles (blue in Fig. 10.9f) undergoes sharp reductions very close to the VP6 thickness, inducing the gradual uncovering of the innermost VP2 (blue arrow in Fig. 10.9f). These experiments not only illustrate a weak interaction between VP6 and VP2 layers, but also a very feeble VP6-VP6 binding energy. Finally, the thin SLP VP2 is highly unstable under fatigue (Fig. 10.9e) experiments collapsing well before reaching 10 frames (green in Fig. 10.9f).

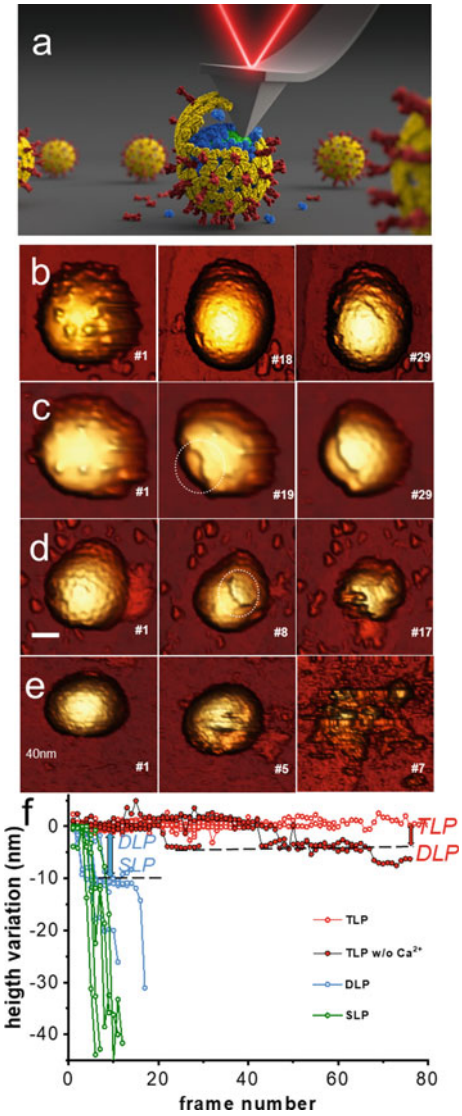

Fig. 10.9 Peeling a virus layer by layer with mechanical fatigue. **a** cartoon of the peeling experiment. Topographic evolution of TLP (**b**), TLP + EDTA (**c**), DLP (**d**) and SLP (**e**) during continuous imaging at low force (~60–120 pN) indicating the corresponding frame. **f** Topographic evolutions obtained at center of each virus particle (**b**–**e**) in TLP (red), DLP (blue) and SLP (green) particles. Dark red color indicates fatigue of TLP + EDTA. Red and blue arrows indicate the loss of height from TLP to DLP and for DLP to SLP, respectively. Adapted from [46]

AFM/fluorescence combination. Here we discuss the methodology for studying the activity of individual nanoreactors based on a protein container. About 220 GFPs are packed inside P22 bacteriophage capsids [47] and its functionality is explored as a function of the mechanical stress applied with the AFM tip to the virus particle while monitoring fluorescence with Total Internal Reflection Fluorescence Microscopy (TIRFM) [48]. The integration of a single molecule fluorescence microscope with AFM requires to monitor the fluorescence signal at the surface to avoid not only the background signal of the AFM probe itself, but also the light coming from the bulk solution (Fig. 10.10a). In this approach [49] P22 bacteriophages are immobilized on a glass surface, in such way that a region with particles visualized with AFM (Fig. 10.10b, left) is correlated with their TIRFM pattern (Fig. 10.10b, right). The diffraction-limited resolution of the optical system restricted the size of the smallest spot to $\lambda/2$ ($\approx$250 nm), which is larger than the P22 VLPs. Consequently, the particles that were too close together (arrow, Fig. 10.10b, left) appeared as a single fluorescence spot (bottom right, Fig. 10.10b, right). The inset of Fig. 10.10b (right) shows the topographic (white) and light (green) profiles of two VLPs (Fig. 10.10b, white and green dotted lines) where the particle width in the fluorescence signal is $\approx$500 nm, approximately five times larger than in the AFM topography. After localizing an intact virus showing fluorescence signal, it is possible to execute a nanoindentation experiment (Fig. 10.10c, black) by using a Si_3N_4 tip to avoid electronic quenching of GFP and isolate pure mechanical effects [49]. The fluorescence remained constant (Fig. 10.10c) during the tip approach (Fig. 10.5a, label 1). Furthermore, the light signal stayed stable even when the tip established contact with the VLP at 1 s and linearly deformed the VLP structure (Fig. 10.10c). Fluorescence quenching started at 1.2 s, coinciding with the force steps that indicated the yielding and/or breaking of the protein shell, reaching a minimum value once the particle stopped collapsing (2 s). At 2.6 s the AFM tip moved backwards, away from the surface, and the fluorescence signal remained stable until the tip was released from the VLP (3 s), coming back to a similar value to the initial magnitude (4 s). This fluoresce reduction is most likely due to changes in the integrity of the packed GFPs. In particular, GFPs can oligomerize inside the P22 cavity (internal radius of 22.2 nm) due to crowding phenomena. In the P22 prohead system there are $\approx$209 GFPs attached internally to the capsid with an, resulting in a nearest neighbor distance of $\approx$3 nm between the protein centers. Since the GFP Stokes radius is 2.8 nm, we derived an average distance of 2 Å between fluorophores. It is possible to simulate the compression of a single P22 particle between two planes (Fig. 10.10d, left). The compressed particle shows that there are around 10 unfolded GFPs inside (Fig. 10.10d, right –red-) which account for the amount of quenched light (Fig. 10.10c, green).

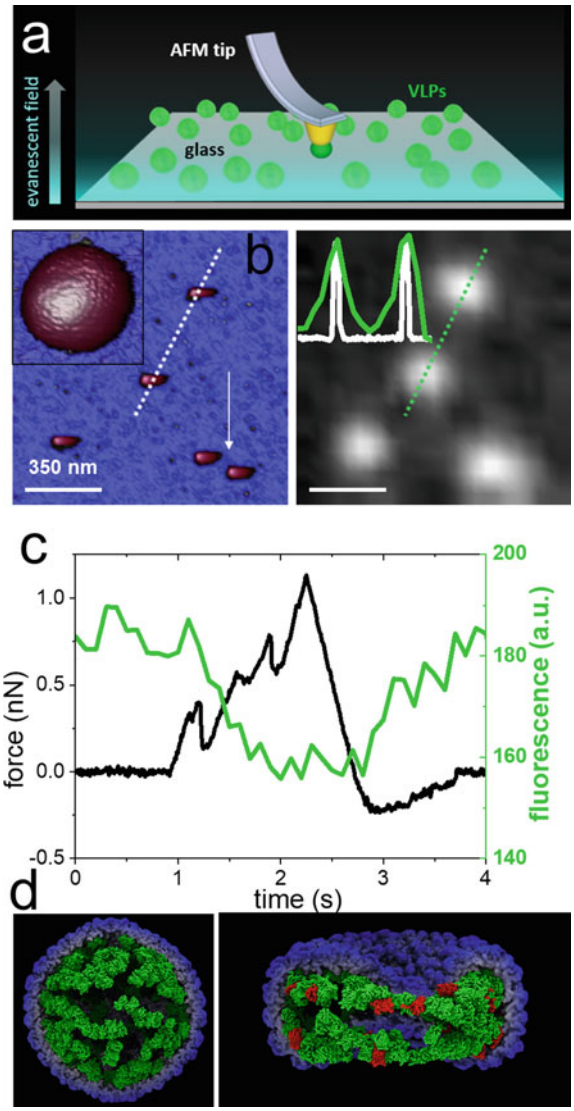

Fig. 10.10 AFM/fluorescence combination: quenching of packed GFP inside P22 protein cages. **a** Presents a diagram of the AFM/TIRF system, showing the P22 VLPs (light green) and the AFM probed particle in dark green. **b** Simultaneous AFM and fluorescence images (right and left, respectively) of individual VLPs on the glass surface. The white arrow (left) indicates a couple of particles appearing as one spot in fluorescence (right). The inset in b-left shows a high-resolution AFM image of P22 VLP resolving the proteinaceous structure of the virus. Inset of b-right compares the lateral resolution of both microscopies by plotting the signal profile of the AFM topography (white) and the fluorescence (green) obtained at the lines indicated by the dashed white and green lines, respectively. **c** Chart representing the simultaneous signals of force (black) and light (green). **d** A simulation of the GFP aggregates (green) inside a P22 procapsid (blue) before deformation (left). In this 3D image, one half of the capsid has been removed to show the internal configuration of the GFPs located below the virus lumen. The right panel shows a deformed virus where the partially unfolded GFPs are highlighted in red. Adapted from [49]

Conclusion and Perspective

Bacteriophage phi29 was the first virus structure to be studied with a scanning probe technique [50], one year before the invention of AFM [51]. A few years later AFM was a generalized technique for studying biological samples [52] at single molecule level. AFM was initially applied just for imaging viruses [53, 54], but it was also used to study the biophysical properties of viruses [9]. During the last 20 years AFM is gradually being considered as a tool for virus research, although is not yet at the level of the classical structure techniques such as electron or X-ray microscopies. Using AFM for measuring the binding forces of virus to cells [55] or for the assembly of 2D virus-like assemblies in real time [56] are also promising applications of AFM that, hopefully, will convince virologists that AFM is an equally valid approach for studying viruses. We hope that the applications of AFM exposed in this chapter will help in this task.

Acknowledgements The authors acknowledge to support by grants received from the Spanish Ministry of Science and Innovation projects (FIS2017-89549-R, FIS2017-90701-REDT and PID2021-126608OB-I00) and the Human Frontiers Science Program (HFSPO RGP0012/2018). IFIMAC is a Center of Excellence "María de Maeztu". J.R.C. acknowledges the Spanish Ministry of Science and Innovation (PID2020-113287RB-I00) and the Comunidad Autónoma de Madrid (P2018/NMT-4389).

References

1. Flint SJ, Enquist LW, Racaniello VR, Skalka AM (2004) Principles of virology. ASM Press, Washington D.C.
2. Douglas T, Young M (1998) Host–guest encapsulation of materials by assembled virus protein cages. Nature 393:152–155. https://doi.org/10.1038/30211
3. Mateu MG (2013) Assembly, stability and dynamics of virus capsids. Arch Biochem Biophys 531:65–79. https://doi.org/10.1016/j.abb.2012.10.015
4. Minton AP (2006) How can biochemical reactions within cells differ from those in test tubes? J Cell Sci 119:2863–2869. https://doi.org/10.1242/jcs.03063
5. Agirre J, Aloria K, Arizmendi JM et al (2011) Capsid protein identification and analysis of mature Triatoma virus (TrV) virions and naturally occurring empty particles. Virology 409:91–101. https://doi.org/10.1016/j.virol.2010.09.034
6. Cordova A, Deserno M, Gelbart WM, Ben-Shaul A (2003) Osmotic shock and the strength of viral capsids. Biophys J 85:70–74. https://doi.org/10.1016/S0006-3495(03)74455-5
7. Baker TS, Olson NH, Fuller SD (1999) Adding the third dimension to virus life cycles: three-dimensional reconstruction of icosahedral viruses from cryo-electron micrographs. Microbiol Mol Biol Rev. https://doi.org/10.1128/MMBR.63.4.862-922.1999
8. Egan P, Sinko R, LeDuc PR, Keten S (2015) The role of mechanics in biological and bio-inspired systems. Nat Commun 6:7418. https://doi.org/10.1038/ncomms8418
9. Ivanovska IL, de Pablo PJ, Ibarra B et al (2004) Bacteriophage capsids: tough nanoshells with complex elastic properties. Proc Natl Acad Sci 101:7600–7605. https://doi.org/10.1073/pnas.0308198101
10. de Pablo PJ (2018) Atomic force microscopy of virus shells. In: Seminars in cell & developmental biology. Academic Press, pp 199–208

11. Müller DJ, Amrein M, Engel A (1997) Adsorption of biological molecules to a solid support for scanning probe microscopy. J Struct Biol 119:172–188. https://doi.org/10.1006/jsbi.1997.3875
12. Zeng C, Hernando-Pérez M, Dragnea B et al (2017) Contact mechanics of a small icosahedral virus. Phys Rev Lett 119:038102. https://doi.org/10.1103/PhysRevLett.119.038102
13. Armanious A, Aeppli M, Jacak R et al (2016) Viruses at solid-water interfaces: a systematic assessment of interactions driving adsorption. Environ Sci Technol 50:732–743. https://doi.org/10.1021/acs.est.5b04644
14. Llauró A, Guerra P, Irigoyen N et al (2014) Mechanical stability and reversible fracture of vault particles. Biophys J 106:687–695. https://doi.org/10.1016/j.bpj.2013.12.035
15. Llauró A, Luque D, Edwards E et al (2016) Cargo–shell and cargo–cargo couplings govern the mechanics of artificially loaded virus-derived cages. Nanoscale 8:9328–9336
16. Zeng C, Hernando-Perez M, Dragnea B et al (2017) Contact Mechanics of a Small Icosahedral Virus. Phys Rev Lett 119:038102. https://doi.org/10.1103/PhysRevLett.119.038102
17. Carpick RW, Ogletree DF, Salmeron M (1997) Lateral stiffness: A new nanomechanical measurement for the determination of shear strengths with friction force microscopy. Appl Phys Lett 70:1548–1550. https://doi.org/10.1063/1.118639
18. Kuznetsov Y, Gershon PD, McPherson A (2008) Atomic force microscopy investigation of vaccinia virus structure. J Virol 82:7551–7566. https://doi.org/10.1128/jvi.00016-08
19. Vinckier A, Heyvaert I, D'Hoore A et al (1995) Immobilizing and imaging microtubules by atomic force microscopy. Ultramicroscopy 57:337–343. https://doi.org/10.1016/0304-3991(94)00194-r
20. Carrasco C, Luque A, Hernando-Pérez M et al (2011) Built-in mechanical stress in viral shells. Biophys J 100:1100–1108. https://doi.org/10.1016/j.bpj.2011.01.008
21. Roos WH (2018) AFM nanoindentation of protein shells, expanding the approach beyond viruses. Semin Cell Dev Biol 73:145–152. https://doi.org/10.1016/j.semcdb.2017.07.044
22. Ortega-Esteban A, Horcas I, Hernando-Perez M et al (2012) Minimizing tip-sample forces in jumping mode atomic force microscopy in liquid. Ultramicroscopy 114:56–61
23. Legleiter J, Park M, Cusick B, Kowalewski T (2006) Scanning probe acceleration microscopy (SPAM) in fluids: mapping mechanical properties of surfaces at the nanoscale. Proc Natl Acad Sci 103:4813–4818. https://doi.org/10.1073/pnas.0505628103
24. Villarrubia JS (1997) Algorithms for scanned probe microscope image simulation, surface reconstruction, and tip estimation. J Res Natl Inst Stand Technol 102:425–454. https://doi.org/10.6028/jres.102.030
25. Horcas I, Fernández R, Gomez-Rodriguez JM, Colchero JW, Gómez-Herrero JW, Baro AM (2007) WSXM: a software for scanning probe microscopy and a tool for nanotechnology. Rev Sci Instrum 78(1):013705. https://doi.org/10.1063/1.2432410
26. Pettersen EF, Goddard TD, Huang CC et al (2004) UCSF Chimera—a visualization system for exploratory research and analysis. J Comput Chem 25:1605–1612. https://doi.org/10.1002/jcc.20084
27. Tang J, Olson N, Jardine PJ et al (2008) DNA poised for release in bacteriophage ø29. Structure 16:935–943. https://doi.org/10.1016/j.str.2008.02.024
28. Risco C, Antón IM, Enjuanes L, Carrascosa JL (1996) The transmissible gastroenteritis coronavirus contains a spherical core shell consisting of M and N proteins. J Virol 70:4773–4777
29. Casanova L, Rutala WA, Weber DJ, Sobsey MD (2009) Survival of surrogate coronaviruses in water. Water Res 43:1893–1898. https://doi.org/10.1016/j.watres.2009.02.002
30. Kiss B, Kis Z, Pályi B, Kellermayer MSZ (2021) Topography, spike dynamics, and nanomechanics of individual native SARS-CoV-2 virions. Nano Lett 21:2675–2680. https://doi.org/10.1021/acs.nanolett.0c04465
31. Perez-Illana M, Martin-Gonzalez N, Hernando-Perez M et al (2021) Acidification induces condensation of the adenovirus core. Acta Biomater 135:534–542. https://doi.org/10.1016/j.actbio.2021.08.019
32. Cantero M, Carlero D, Chichón FJ et al (2022) Monitoring SARS-CoV-2 surrogate TGEV individual virions structure survival under harsh physicochemical environments. Cells 11:1759. https://doi.org/10.3390/cells11111759

33. Zink M, Grubmüller H (2009) Mechanical properties of the icosahedral shell of southern bean mosaic virus: a molecular dynamics study. Biophys J 96:1350–1363. https://doi.org/10.1016/j.bpj.2008.11.028
34. Ortega-Esteban Á, Mata CP, Rodríguez-Espinosa MJ et al (2020) Cryo-electron microscopy structure, assembly, and mechanics show morphogenesis and evolution of human picobirnavirus. J Virol 94:e01542-e1620. https://doi.org/10.1128/JVI.01542-20
35. Landau Theory of Elasticity - 3rd Edition. https://www.elsevier.com/books/theory-of-elasticity/landau/978-0-08-057069-3?country=ES&format=print&utm_source=google_ads&utm_medium=paid_search&utm_campaign=spainshopping&gclid=CjwKCAiAv9ucBhBXEiwA6N8nYFtCfz0HTtRL1L1syWMEHTtv-UorKaSJ__wX7OwicfFg6RH2LwSclRoCE24QAvD_BwE&gclsrc=aw.ds. Accessed 12 Dec 2022
36. Katen S, Zlotnick A (2009) The Thermodynamics of virus capsid assembly. Methods Enzymol 455:395–417. https://doi.org/10.1016/S0076-6879(08)04214-6
37. Ortega-Esteban A, Condezo GN, Pérez-Berná AJ et al (2015) Mechanics of viral chromatin reveals the pressurization of human adenovirus. ACS Nano 9:10826–10833
38. Martín-González N, Hernando-Pérez M, Condezo GN et al (2019) Adenovirus major core protein condenses DNA in clusters and bundles, modulating genome release and capsid internal pressure. Nucleic Acids Res 47:9231–9242
39. Yao H, Song Y, Chen Y et al (2020) Molecular architecture of the SARS-CoV-2 virus. Cell 183:730-738.e13. https://doi.org/10.1016/j.cell.2020.09.018
40. Petrov AS, Boz MB, Harvey SC (2007) The conformation of double-stranded DNA inside bacteriophages depends on capsid size and shape. J Struct Biol 160:241–248. https://doi.org/10.1016/j.jsb.2007.08.012
41. Greber UF, Willetts M, Webster P, Helenius A (1993) Stepwise dismantling of adenovirus 2 during entry into cells. Cell 75:477–486
42. Zhou H-X, Rivas G, Minton AP (2008) Macromolecular crowding and confinement: biochemical, biophysical, and potential physiological consequences. Annu Rev Biophys 37:375–397. https://doi.org/10.1146/annurev.biophys.37.032807.125817
43. Hernando-Pérez M, Lambert S, Nakatani-Webster E et al (2014) Cementing proteins provide extra mechanical stabilization to viral cages. Nat Commun 5:1–8
44. Ortega-Esteban A, Pérez-Berná AJ, Menéndez-Conejero R et al (2013) Monitoring dynamics of human adenovirus disassembly induced by mechanical fatigue. Sci Rep 3:1434. https://doi.org/10.1038/srep01434
45. Martín-González N, Delgado-Buscalioni R, de Pablo PJ (2021) Long-range cooperative disassembly and aging during adenovirus uncoating. Phys Rev X 11:021025
46. Jiménez-Zaragoza M, Yubero MP, Martín-Forero E et al (2018) Biophysical properties of single rotavirus particles account for the functions of protein shells in a multilayered virus. eLife 7:e37295. https://doi.org/10.7554/eLife.37295
47. O'Neil A, Prevelige PE, Basu G, Douglas T (2012) Coconfinement of fluorescent proteins: spatially enforced communication of GFP and mCherry encapsulated within the P22 capsid. Biomacromol 13:3902–3907. https://doi.org/10.1021/bm301347x
48. Ortega-Esteban A, Bodensiek K, San Martín C et al (2015) Fluorescence tracking of genome release during mechanical unpacking of single viruses. ACS Nano 9:10571–10579
49. Strobl K, Selivanovitch E, Ibáñez-Freire P et al (2022) Electromechanical photophysics of GFP packed inside viral protein cages probed by force-fluorescence hybrid single-molecule microscopy. Small 18:2200059. https://doi.org/10.1002/smll.202200059
50. Baró AM, Miranda R, Alamán J et al (1985) Determination of surface topography of biological specimens at high resolution by scanning tunnelling microscopy. Nature 315:253–254. https://doi.org/10.1038/315253a0
51. Binnig G, Quate CF, Gerber Ch (1986) Atomic force microscope. Phys Rev Lett 56:930–933. https://doi.org/10.1103/PhysRevLett.56.930
52. Bustamante C, Vesenka J, Tang CL et al (1992) Circular DNA molecules imaged in air by scanning force microscopy. Biochemistry 31:22–26. https://doi.org/10.1021/bi00116a005

53. Day J, Kuznetsov YG, Larson SB et al (2001) Biophysical studies on the RNA cores of satellite tobacco mosaic virus. Biophys J 80:2364–2371. https://doi.org/10.1016/S0006-3495(01)76206-6
54. Drygin YF, Bordunova OA, Gallyamov MO, Yaminsky IV (1998) Atomic force microscopy examination of tobacco mosaic virus and virion RNA. FEBS Lett 425:217–221. https://doi.org/10.1016/S0014-5793(98)00232-4
55. Alsteens D, Newton R, Schubert R et al (2017) Nanomechanical mapping of first binding steps of a virus to animal cells. Nat Nanotechnol 12:177–183. https://doi.org/10.1038/nnano.2016.228
56. Valbuena A, Maity S, Mateu MG, Roos WH (2020) Visualization of single molecules building a viral capsid protein lattice through stochastic pathways. ACS Nano 14:8724–8734